RSC Advances

PAPER

View Article Online
View Journal | View Issue

Cite this: *RSC Adv.*, 2020, **10**, 6121

Three-dimensional microspheric g-C_3N_4 coupled by *Broussonetia papyrifera* biochar: facile sodium alginate immobilization and excellent photocatalytic Cr(VI) reduction

Qi Jin,[a] Guangyu Xie,[b] Xiaoxi Cai,[c] Xinjiang Hu,*[b] Hui Wang,[b] Guoqiang Qiu,[a] Weixuan Wang,[d] Daixi Zhou,[b] Huiwen Huo,[b] Xiaofei Tan[ef] and Yunlin Zhao*[ab]

Received 28th November 2019
Accepted 14th January 2020

DOI: 10.1039/c9ra09981f

rsc.li/rsc-advances

Photocatalysts comprising *Broussonetia papyrifera* biochar and g-C_3N_4 loaded on sodium alginate were prepared and characterized in terms of reusability and photocatalytic Cr(VI) reduction performance. The observed photocurrent responses as well as photoluminescence and UV-visible diffuse reflectance spectra showed that the best-performing catalyst featured the benefits of efficient photogenerated charge separation, superior electron conductance/transfer, and excellent light adsorption ability, which resulted in a higher photocatalytic Cr(VI) reduction performance compared to that of pure g-C_3N_4 powder. The prepared composite was shown to be reusable and well separable from the reaction mixture, thus being a promising material for the practical photocatalytic removal of Cr(VI) from wastewater. The trapping experiment and XPS spectra of catalysts after reactions confirm that the decontamination of Cr(VI) lies in the photocatalytic reduction of this species into low-toxicity Cr(III) by photoinduced electrons generated from g-C_3N_4, followed by the adsorption of Cr(III) on biochar or alginate with large specific areas.

1 Introduction

Cr is extensively used in tanning, electroplating, dyeing, and the manufacture of medicines and preservatives.[1] However, the high redox potential and excellent solubility of this essential element can cause serious environmental pollution and threaten human health if Cr-contaminated wastewaters (mainly containing Cr(VI) and Cr(III)) are not properly treated.[2] As the toxicity of the carcinogenic and mutagenic Cr(VI) exceeds that of Cr(III) more than 100-fold, Cr removal is mainly performed by electrolytic, chemical (with Fe^0), or photocatalytic reduction of Cr(VI) to Cr(III) and the elimination of the latter as insoluble $Cr(OH)_3$ in alkaline solutions.[3,4] Among these methods, photocatalytic reduction features the advantages of operation simplicity, mild conditions, high cost-efficiency, catalyst recyclability, use of sustainable solar energy, non-toxicity, and technological maturity, and is therefore viewed as the method of choice.[5,6]

Photocatalysis refers to the reaction of photogenerated charges and reactive free radicals with pollutants to realize decontamination, and the fabrication of high-efficiency photocatalysts is therefore vital for improving photocatalytic performance.[7,8] TiO_2 is a popular photocatalyst because of its nontoxicity, chemical stability, low cost, and impressive photoactivity;[9] however, this material has a comparatively wide bandgap and, hence, a shortened optical response range.[10,11] Consequently, photocatalysts active in the visible-light range are highly sought after. Among such catalysts, g-C_3N_4 (bandgap = 2.7 eV) is a novel metal-free photoactive material with a two-dimensional layered aromatic polycyclic structure comprising sp^2-hybridized C and N atoms and featuring C–N bonds of uniform length.[12–14] At present, g-C_3N_4 is used as a visible-light photocatalyst for the degradation of organic pollutants, semi-reaction of H_2/O_2 evolution, complete water splitting, CO_2 reduction, and organic synthesis.[15–19] However, its widespread application is hindered by the high rate of photogenerated electron–hole pair recombination.[20]

Biochar, a carbonaceous solid with excellent adsorption ability, is obtained by high-temperature anaerobic pyrolysis of biomass and is used in composites with g-C_3N_4 to realize more

[a]*Faculty of Life Science and Technology, Central South University of Forestry and Technology, Changsha 410004, P.R. China. E-mail: zyl8291290@163.com; Tel: +8613548945666*

[b]*College of Environmental Science and Engineering, Central South University of Forestry and Technology, Changsha 410004, P.R. China. E-mail: huxinjiang@126.com; Tel: +8615243694564*

[c]*College of Art and Design, Hunan First Normal University, Changsha 410205, P.R. China*

[d]*College of Geography and Environmental Science, Northwest Normal University, Lanzhou 730070, P.R. China*

[e]*College of Environmental Science and Engineering, Hunan University, Changsha 410082, P.R. China*

[f]*Key Laboratory of Environmental Biology and Pollution Control (Hunan University), Ministry of Education, Changsha 410082, P.R. China*

efficient visible light adsorption, faster electron transfer, slower electron–hole recombination, and higher surface area.[21,22] Yan *et al.* ascribed the enhanced photocatalytic performance of carbon/g-C_3N_4 composites to the high electron conductivity of residual carbon, while Li *et al.* prepared biochar-coupled g-C_3N_4 from *Camellia oleifera* shells and melamine, revealing that these composites feature an increased Cr(VI) adsorption capacity and reduction ability due to their large specific surface area and superior electron conduction.[23,24] *Broussonetia papyrifera*, a deciduous tree mainly found in Asian countries such as China and Japan, exhibits the advantages of fast growth, easy proliferation, and great disease resistance, which makes the utilization of its fallen leaves (*e.g.*, by pyrolysis) a task of high practical importance.[25,26] Biochar prepared from the fallen leaves of *B. papyrifera* features a pore structure and surface chemistry similar to those of activated carbon, possesses excellent adsorption ability, and is cheap to produce.[27,28] Herein, *B. papyrifera* biochar was combined with g-C_3N_4 to enhance its photocatalytic performance by suppressing the recombination of photogenerated electron–hole pairs.

The practical application of numerous photocatalysts for water purification is hindered by their poor recyclability and reusability, especially in cases when these materials are applied as powders.[29] Sodium alginate, a polysaccharide extracted from brown algae and also known as alginate gel, features the benefits of bioavailability, nontoxicity, and the ability to immobilize various substances.[30] The exchange of Na^+ in sodium alginate for divalent cations such as Ca^{2+}, Cu^{2+}, and Ba^{2+} results in the formation of stable biopolymers with a unique three-dimensional structure.[31] Herein, g-C_3N_4 powder and biochar prepared from *B. papyrifera* fallen leaves were immobilized on sodium alginate to prepare photoactive biochar-coupled g-C_3N_4 (SABC), and the structure, morphology, and optical properties of this composite were probed by several instrumental techniques. The effects of electron conductivity and heterojunction charge separation were analyzed by photoluminescence spectroscopy and photocurrent density measurements, and Cr(VI) photoreduction experiments under visible-light illumination were carried out to demonstrate the excellent photocatalytic performance of the above heterojunction.

2 Materials and methods

2.1 Synthesis of SABC

Melamine (20 g) was loaded into a crucible and sequentially soaked by ultrapure water and ethanol and the supernatant were removed. The crucible was then heated at muffle furnace to 80 °C to evaporate ethanol, and further heated at 600 °C for 4 h to afford a light-yellow solid that was ground to obtain g-C_3N_4 powder.

B. papyrifera leaves (harvested from a manganese mine in Xiangtan City, Hunan Province) were washed, dried, crushed, and sieved to obtain powders, which were then loaded into a corundum boat, placed into a tubular furnace, and pyrolyzed at 500 °C at a heating rate of 7 °C min^{-1} under a continuous flow of nitrogen. After 2 h pyrolysis, the furnace was cooled to 25 °C to obtain *B. papyrifera* biochar.

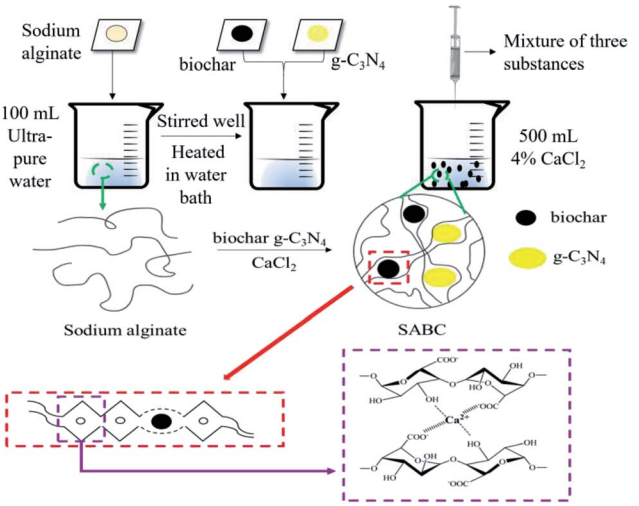

Scheme 1 Representation of the preparation of photocatalytic microspheres.

Sodium alginate (1.5 g) was dissolved in ultrapure water (100 mL) upon heating in a water bath, and the obtained solution was charged with different amounts of g-C_3N_4 and *B. papyrifera* biochar. The resulting mixtures were uniformly stirred, dropwise added to 4 wt% aqueous $CaCl_2$ using injectors, and allowed to react for 4 h to obtain SABC microspheres, with SABC-1, SABC-2, and SABC-3 corresponding to biochar : g-C_3N_4 mass ratios of 1 : 1, 1 : 2, and 2 : 1, respectively (Scheme 1). Pure sodium alginate (SA), sodium alginate-biochar (SAB), and sodium alginate-g-C_3N_4 (SAC) samples were prepared for comparison.

2.2 Characterization

The Brunauer–Emmett–Teller (BET) surface area was measured with BET ratio surface and aperture analyzer (NOVA2000e, Quantachrome, USA). Scanning electron microscopy (SEM) and X-ray energy-dispersive spectroscopy (EDX) analyses were performed using a QUANTA250 scanning electron microscope (FEI, USA) equipped with an X-MAX-50 EDX module (INCA, UK). Crystal phase composition was probed by X-ray diffraction (XRD; D/max-2500 and Smartlab9K, Rigaku, Japan), and surface functional groups were identified by Fourier transform infrared (FTIR) spectroscopy (NICOLET 5700, Thermo Nicolet Corp., USA). The valence states of surface elements were determined by X-ray photoelectron spectroscopy (XPS; ESCALAB 250Xi, Thermo Fisher Scientific, USA), and photoluminescence (PL) spectra were observed at an FLS 980 fluorescence spectrophotometer (Edinburgh Instruments, UK). Photocurrents were measured on a CHI760E electrochemical workstation, and light adsorption ability was probed by UV-vis spectrophotometry (U-4100, Hitachi, Japan). Electron signals generated in illuminated materials were detected by electron spin resonance (ESR; JES FA200, JEOL, Japan).

2.3 Photoelectrochemical measurements

The photocurrent intensity of the materials was measured using a CHI760E electrochemical workstation *via* a three-electrode

model. It consists of the Ag/AgCl electrode in the KCl solution, Pt electrode and a working electrode that were prepared by dropping 0.1 mL of sludge on a 1 × 2 cm FTO substrate. The sludge was made by dispersing 20 mg of materials in 2 mL 0.25% Nafion. The electrolyte solution used in this system is 0.5 M Na_2SO_4. The light source is the same as that in the photocatalytic experiments.

2.4 Photocatalytic activity test

A Cr(VI) stock solution (1 g L^{-1}) was obtained as follows. Potassium dichromate dried to constant mass (2.829 g) was dissolved in ultrapure water, and the solution was transferred into a volumetric flask and made up to 1000 mL. Variable-concentration solutions of Cr(VI) were prepared by stock solution dilution. The photocatalytic reduction of Cr(VI) by SABC microspheres was investigated under visible-light illumination using a 300 W Xe lamp (CEL-HXF300) with a UV cutoff filter as a visible light source. Typically, a solution of Cr(VI) (100 mL, 50 mg L^{-1}) was placed in a beaker, treated with NaOH or HCl for pH adjustment (at 2.0), and charged with the photocatalyst under investigation (4 g wet weight). The mixture was magnetically stirred under visible light irradiation, and 4 mL aliquots were withdrawn every 30 min to measure the concentration of Cr(VI) by UV spectrophotometry at a wavelength of 540 nm.

3 Results and discussion

3.1 Characterizations

3.1.1 Surface characteristics and micromorphology. The BET surface area of SA, SAB, SAC and SABC microspheres had been tested (Table 1). The comparison between SA and SAB indicates the adding of *B. papyrifera* biochar effectively increased the surface areas. Notably, among all coupling materials, SABC-3 possesses the highest surface area, suggesting that SABC-3 may show the superior adsorption capacity. Fig. 1a shows a SEM image of SABC-3, revealing that this composite comprised microspheres approximately 1500 μm in diameter, which facilitated their separation after the photocatalytic reaction. The presence of numerous wrinkles on the microsphere surface implied the good mixing of g-C_3N_4 and biochar, which, in turn, provided an increased number of Cr(VI) adsorption sites and improved the synergy between adsorption and photocatalytic activity. The element mapping in Fig. 1b–e show that C, N, and O were uniformly distributed on the surface of SABC-3.

Table 1 The BET surface area of SA, SAB, SAC and SABC microspheres

Composites	SA	SAB	SAC	SABC-1	SABC-2	SABC-3
Surface area (m^2 g^{-1})	6.958	8.472	0.548	1.148	3.677	10.051

3.1.2 XRD. In our previous study, the XRD patterns of the g-C_3N_4 showed two characteristic peaks at 13.0° and 27.4°, corresponding to reflections from the (100) and (102) crystal planes of g-C_3N_4 (JCPDS 87-1526), respectively.[32,33] XRD analysis (Fig. 2a) showed that the pattern of SAC featured two characteristic peaks that are same as that of g-C_3N_4.[34] As expected, the above peaks were also observed for SABC, which confirmed the presence of g-C_3N_4 therein.

3.1.3 FTIR. Fig. 2b shows the FTIR spectra of SA, SAB, SAC, and SABC microspheres. The SA peak around 3446 cm^{-1} was ascribed to the stretching vibration of –OH groups, while peaks at 1643 and 1424 cm^{-1} were attributed to the symmetric and antisymmetric stretching vibrations of carboxylate anions (COO^-), respectively.[35] The spectrum of SAB was similar to that of SA, which indicated that biochar contained abundant active functional groups such as –COOH and –OH. As for SAC, the peaks at ~808, 1200–1600, and ~1643 cm^{-1} were attributed to the C–N out-of-plane bending vibration, typical aromatic C–N stretching vibration, and the C=N stretching vibration of g-C_3N_4, respectively.[36–38] The similar peak patters in SABC spheres as SA, SAB, and SAC implies the successful preparation of g-C_3N_4 and biochar composite immobilized into alginate.

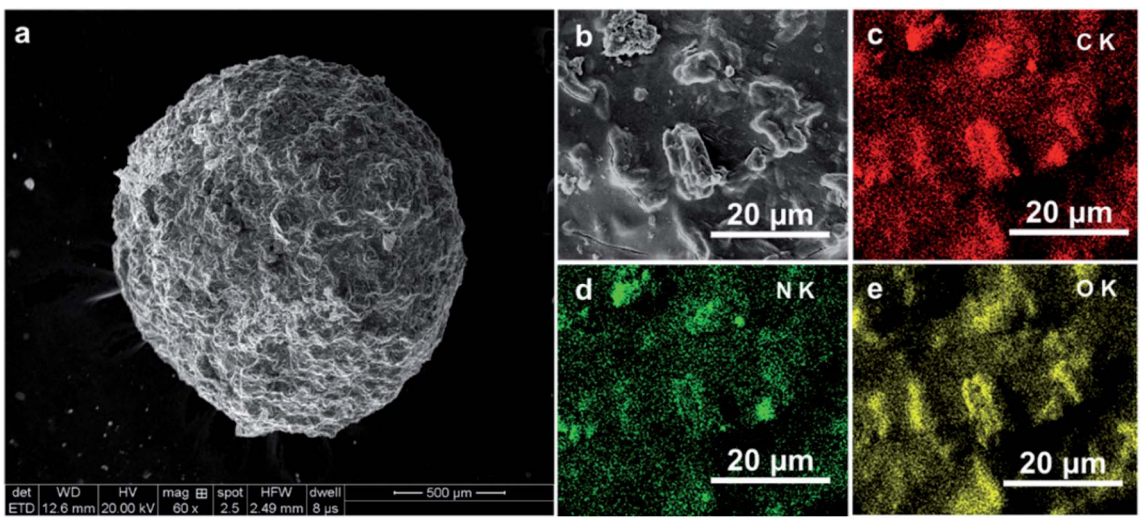

Fig. 1 (a) SEM images of SABC-3 microspheres; and (b–e) corresponding elemental mapping images of C, N, and O.

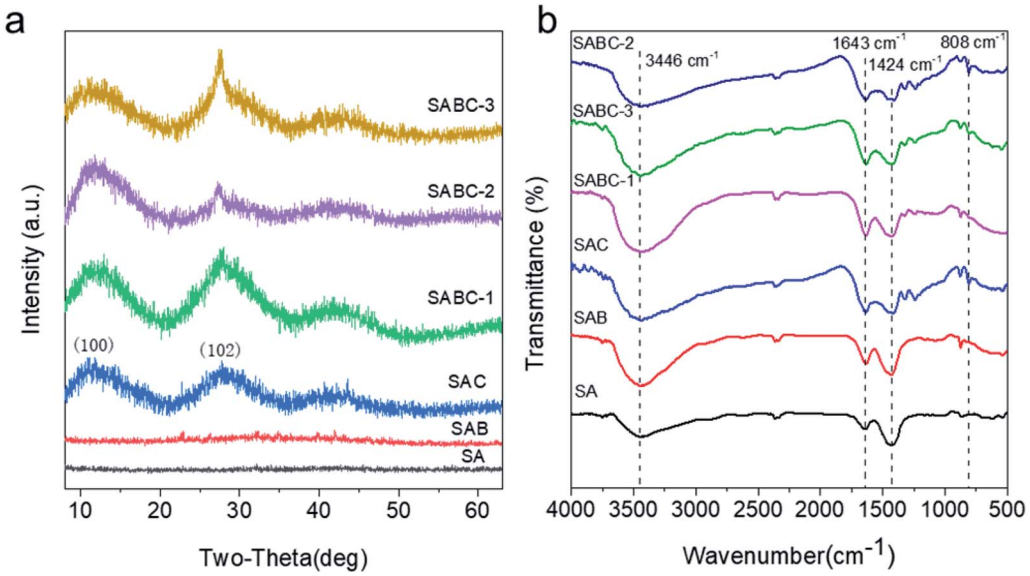

Fig. 2 (a) XRD patterns and (b) FTIR spectra of SA, SAB, SAC and SABC microspheres.

3.1.4 XPS. XPS is an effective analytical method for qualitative and quantitative determination elements on the surface of materials and their structural identification.[39] The C 1s, N 1s, and O 1s spectra of SABC-3 microspheres are shown in Fig. 3a–c, respectively. C1s of SABC-3 in Fig. 3a can be deconvoluted into 6 peaks, at 284.61, 284.81, 285.30, 286.72, 288.21, and 289.00 eV, belonging to C–N, C–C, C–O, C–O–C, N–C=N and O–C=O units, respectively.[32,33] The N1s spectrum shown in Fig. 3b can

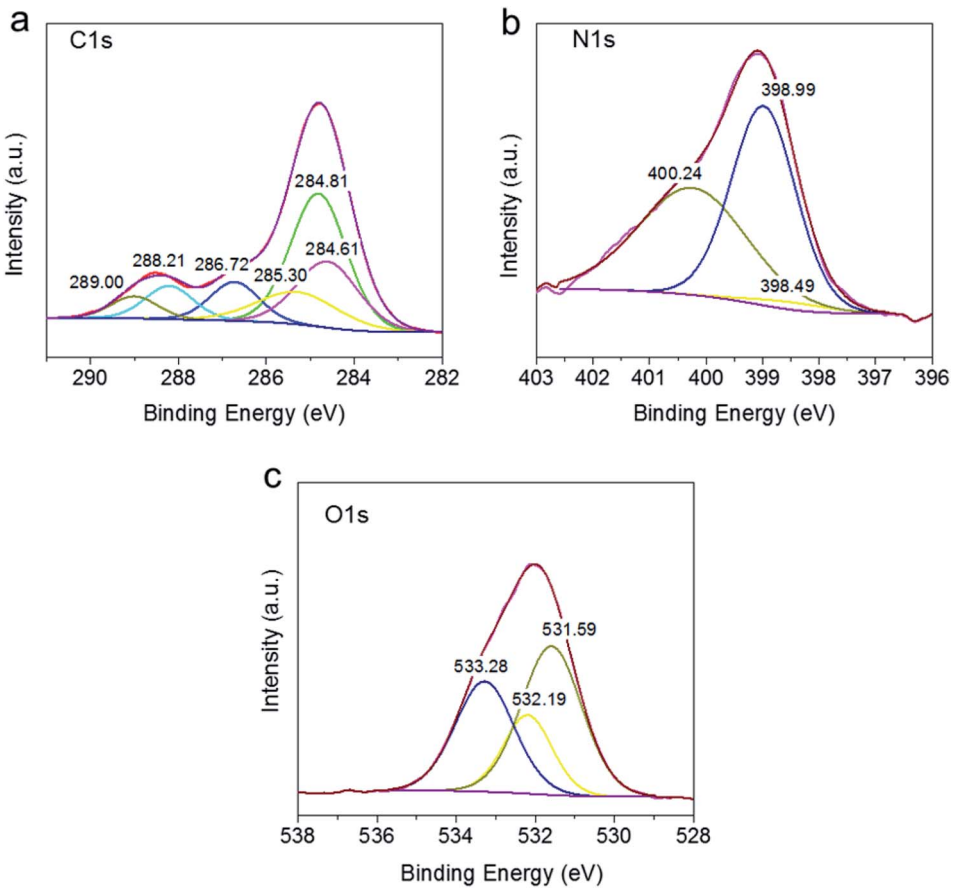

Fig. 3 High-resolution spectra of (a) C 1s, (b) N 1s and (c) O 1s of SABC-3.

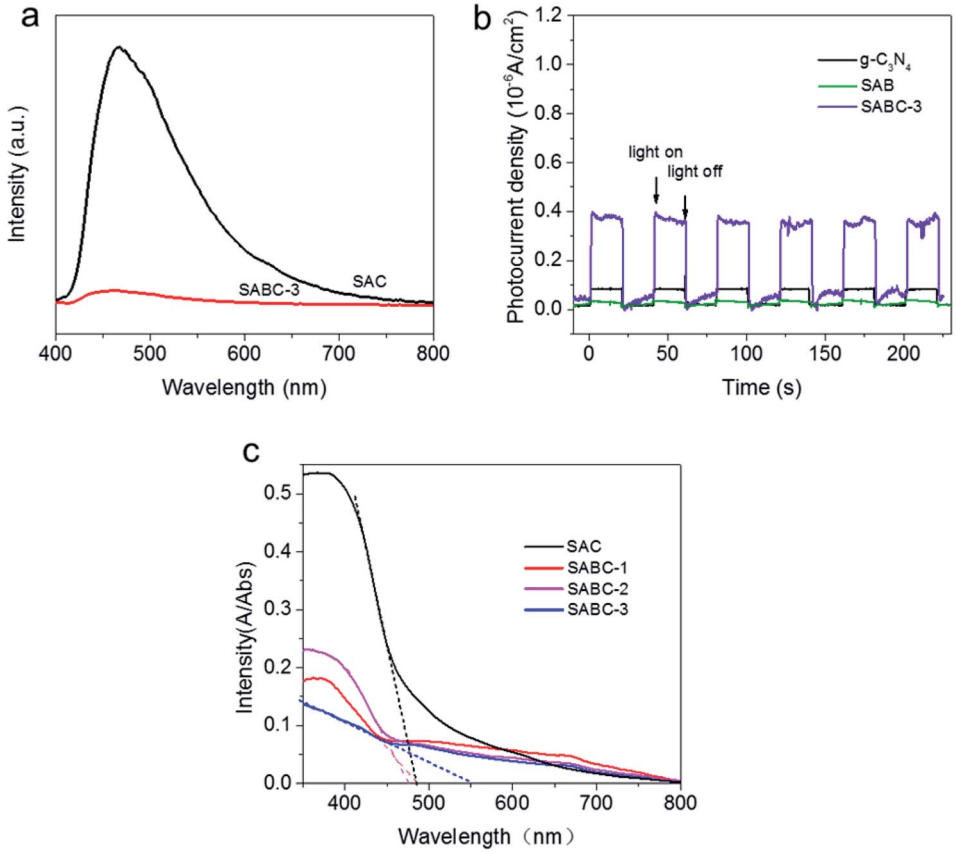

Fig. 4 (a) PL spectra of SAC and SABC-3 microspheres; (b) Photocurrent response density of g-C_3N_4, SAB and SABC-3 microspheres; (c) UV-vis spectra of SAC and SABC microspheres.

be deconvoluted into peaks at 398.49, 398.99, and 400.24 eV, belonging to C–N=C, C–N, and N-$(C)_3$.[34,40] From Fig. 3c, the O 1s spectrum featured the contributions of –OH (531.27 eV), C–O (532.19 eV), and O–C=O (533.28 eV) moieties.[41–43] The above results indicated that the composite possessed a sufficient number of active groups on its surface, which was expected to increase pollutant removal efficiency.

3.2 Charge separation and optical properties

PL spectroscopy probes the separation efficiency of photogenerated carriers in a given photocatalyst, with more intense PL signals indicating lower separation efficiency and more efficient carrier recombination.[44] Fig. 4a shows that the PL signal of SAC was much more intense than that of SABC-3,

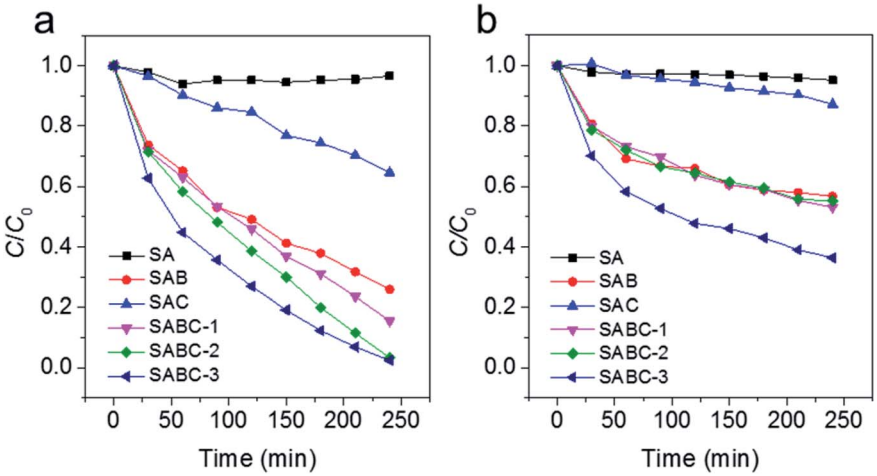

Fig. 5 (a) Photoreduction of Cr(VI) by SA, SAB, SAC and SABC microspheres under visible light irradiation; (b) adsorption of Cr(VI) by SA, SAB, SAC and SABC microspheres: [Cr(VI)] = 50 mg L^{-1}, m = 40 g L^{-1}, pH = 2.0.

indicating that biochar addition greatly suppressed electron–hole pair recombination. The peak of SABC-3 was slightly shifted relative to that of SAC, which indicated an interaction between g-C_3N_4 and biochar. Thus, biochar addition was concluded to facilitate charge transfer and diffusion in the composite to effectively inhibit the recombination of photogenerated electron–hole pairs and enhance photocatalytic performance.[45]

Fig. 4b presents the photocurrent responses of as-prepared materials, showing that g-C_3N_4, SAB, and SBC-3 featured stable photocurrents under visible-light illumination yet exhibited different photocurrent intensities. The lowest and highest photocurrents were observed for SAB and SABC-3, respectively, and the latter composite was therefore concluded to offer the highest photoelectric conversion efficiency, mainly due to the promotional effect of biochar on the separation of photogenerated carriers. These results further proved that the combination of alginate, g-C_3N_4, and *B. papyrifera* biochar improved photocatalytic performance.

The optical properties of photocatalytic materials determine their light absorption ability, which profoundly impacts photoelectrochemical properties and photocatalytic performance. Herein, the optical properties of SAC and SABC microspheres were probed by UV-vis diffuse reflectance spectroscopy (Fig. 4c). The slight red shift of the absorption band edge of SABC-3 (~550 nm) compared to that of SAC (485 nm) indicated that the former material could efficiently absorb low-energy light and thus effectively utilize light energy to produce more electron–hole pairs and thus increase photocatalytic performance.

3.3 Photoreduction of Cr(VI)

3.3.1 Optimization of SABC microspheres. Fig. 5a compares the Cr(VI) photocatalytic reduction performances of SA, SAB, SAC, and SABC microspheres, while Fig. 5b compares the corresponding adsorption capacities. SA showed almost no photocatalytic Cr(VI) removal activity after 240 min, *i.e.*, the interaction between pure alginate and Cr(VI) was weak. SAC featured a weak ability for photocatalytic Cr(VI) reduction, achieving a removal efficiency of only 35% because of serious photogenerated carrier recombination and poor adsorption ability of g-C_3N_4. Compared to SA and SAC, SAB had a higher Cr(VI) adsorption capacity, *i.e.*, featured more active surface sites capable of Cr(VI) capture. This increased adsorption capacity provided the basis for electron transfer during photocatalytic reduction. Fig. 5a shows that the photocatalytic activity of SABC for Cr(VI) reduction was significantly higher than that of SA, SAB, and SAC. Among the SABC samples, the best performance was observed for SABC-3, mainly because of its high biochar content, which facilitated Cr(VI) adsorption and the transmission of photogenerated electrons to suppress the recombination of electron–hole pairs.

3.3.2 Reuse of SABC-3. The results of SABC-3 recyclability tests are presented in Fig. 6. After the completion of a photocatalytic cycle, SABC-3 was collected using plastic spoons, washed with ultrapure water, and soaked in 4 wt% aqueous $CaCl_2$ to initiate the next cycle. High photocatalytic

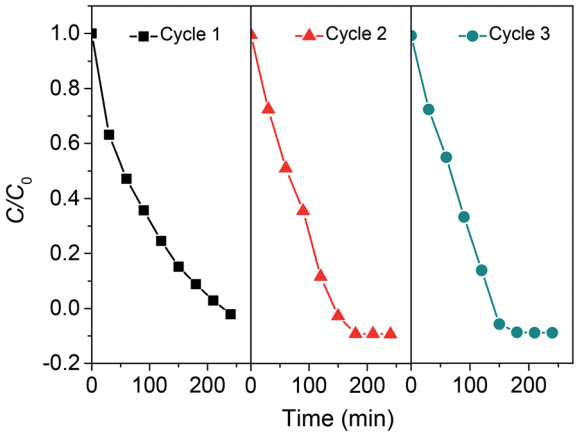

Fig. 6 Recycle experiments of SABC-3 microspheres for photoreduction of Cr(VI): [Cr(VI)] = 50 mg L^{-1}, m = 40g L^{-1}, pH = 2.

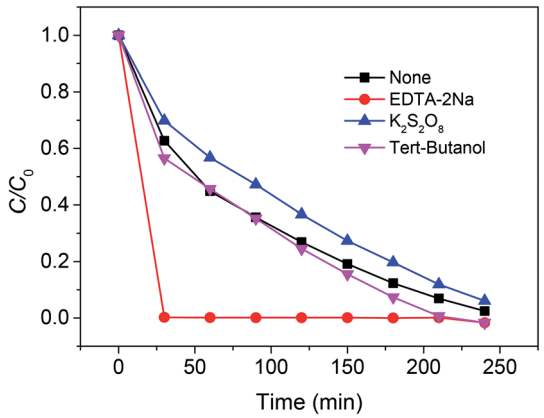

Fig. 7 Trapping experiments for the photoreduction of Cr(VI) over SABC-3 microspheres under visible light irradiation: [Cr(VI)] = 50 mg L^{-1}, m = 40 g L^{-1}, pH = 2.0.

performance was retained for the three cycles performed in total, and the above composite was concluded to be reusable, recyclable, and well suited for practical cost-effective photocatalytic water purification.

3.4 Photocatalytic reaction mechanism

To study the contribution of different active species to the Cr(VI) photoreduction by SABC-3, photoreduction was performed in the presence of three typical scavengers (*tert*-butanol (TBA), $K_2S_2O_8$, and EDTA-2Na, 0.01 M each) to quench ··OH, electrons, and holes, respectively.[32] Fig. 7 shows that the Cr(VI) decontamination was inhibited in the presence of $K_2S_2O_8$, indicating that electrons play an important role in the photocatalytic reduction process. The addition of TBA did not have a significant effect, *i.e.*, hydroxyl radicals were not largely involved in the photocatalytic process. Notably, the reaction rate dramatically increased in the presence of EDTA-2Na, mainly because of the removal of holes to inhibit electron–hole recombination and allow more electrons to participate in Cr(VI) photoreduction process. The above results further illustrate that

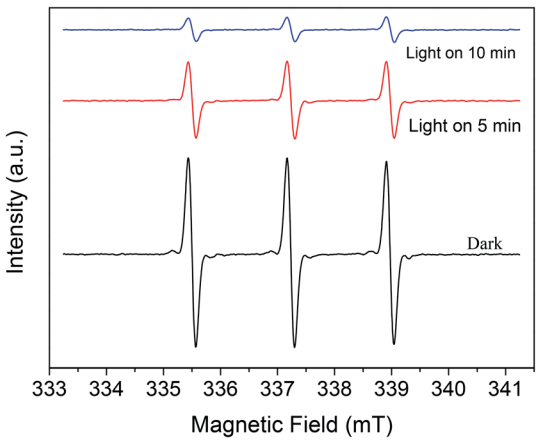

Fig. 8 ESR spectra of TEMPO in the dark and under visible light irradiation.

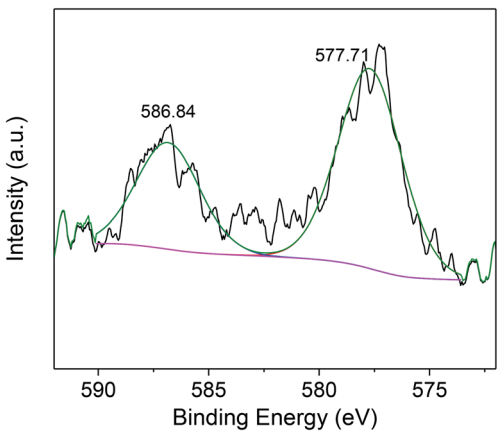

Fig. 9 High-resolution spectra of Cr 2p on SABC-3 microspheres surface after irradiation.

photogenerated e^- are the main active substances in the photocatalytic reduction process.

Since photogenerated electrons are essential active species in the photocatalytic process, the ESR test was performed on SABC-3 to qualify the generation of electrons under visible-light irradiation according to the detected signal intensity and the result was shown in Fig. 8. The intensity of ESR signals represents the electron scavenger concentration, *i.e.*, is negatively correlated with electron content. In the dark, the signal intensity was high (*i.e.*, few electrons were generated), decreasing upon irradiation with visible light, *i.e.*, upon the increase of the number of electrons in the reaction system. Thus, a large number of electrons could be generated in SABC-3 upon illumination with visible light to reduce Cr(VI) in the solution.

After the photocatalytic reaction, SABC-3 microspheres were probed by XPS (Fig. 9). The deconvoluted peaks at 577.71 and 586.84 eV were ascribed to Cr $2p_{3/2}$ and Cr $2p_{1/2}$ spectra of Cr(III) ions, which implied that the Cr(VI) is completely reduced to Cr(III) by electrons generated by g-C_3N_4.[46,47] Finally, the produced Cr(III) species are captured by biochar or alginate on SABC-3 to achieve decontamination.

4 Conclusions

Biochar-coupled g-C_3N_4 microspheres (SABC) were prepared by immobilization of g-C_3N_4 and *B. papyrifera* biochar on alginate. The obtained microspheres featured excellent photocatalytic performance for Cr(VI) reduction, could be easily separated and recycled, and were therefore well suited for practical photocatalytic water purification. The mechanism of Cr(VI) reduction was elucidated by photoelectrochemical measurements and optical property tests, which revealed that g-C_3N_4 generates a sufficient amount of electron–hole pairs upon visible-light irradiation, while biochar accelerates the transfer of electrons and promotes their separation from holes. The composite with the largest biochar content (SABC-3) featured the fastest Cr(VI) adsorption and photocatalytic reduction rate, *i.e.*, the addition of *B. papyrifera* biochar promoted adsorption and electron transmission. Cycling experiments revealed the high recyclability of the prepared composite microspheres. Photogenerated electrons were found to be the main active species in this photocatalytic system, and the reduced Cr(III) could be removed by adsorption on biochar or alginate.

Conflicts of interest

There are no conflicts to declare.

Acknowledgements

This study was financially supported by the National Natural Science Foundation of China (Grant No. 51979294, 51608208), the Natural Science Foundation of Hunan Province (Grant No. 2018JJ3887, 2019JJ51005 and 2018JJ3096), the Research Foundation of Education Department of Hunan Province, China (Grant No. 17K105), the Training Program for Excellent Young Innovators of Changsha (Grant No. kq1905064), the Key Research and Development Program of Hunan Province, China (Grant No. 2019SK2191).

References

1 E. Malkoc, Y. Nuhoglu and Y. Abali, *Chem. Eng. J.*, 2006, **119**, 61–68.
2 S. Xu, J. Dai, J. Yang, J. You and J. Hao, *Nanomaterials*, 2018, **8**, 472–489.
3 M. A. Ahsan, S. K. Katla, M. T. Islam, J. A. Hernandez-Viezcas, L. M. Martinez, C. A. Díaz-Moreno, J. Lopez, S. R. Singamaneni, J. Banuelos, J. Gardea-Torresdey and J. C. Noveron, *Environmental Technology & Innovation*, 2018, **11**, 23–40.
4 J. Ren, G. Zhang, D. Wang, D. Cai and Z. Wu, *Bioresour. Technol.*, 2019, **291**, 121856–121862.
5 G. C. Zhang, J. Zhong, M. Xu, Y. Yang, Y. Li, Z. Fang, S. Tang, D. Yuan, B. Wen and J. Gu, *Chem. Eng. J.*, 2019, **375**, 122093–122102.
6 C. Xue, D. Li, Y. Li, N. Li, F. Zhang, Y. Wang, Q. Chang and S. Hu, *Ceram. Int.*, 2019, **45**, 17512–17520.

7 J. Li, P. Yan, K. Li, W. Cen, X. Yu, S. Yuan, Y. Chu and Z. Wang, *Chin. J. Catal.*, 2018, **39**, 1695–1703.
8 S. Wang, X. Zhang, L. Pan, F.-M. Zhao, J.-J. Zou, T. Zhang and L. Wang, *Appl. Catal., B*, 2015, **164**, 234–240.
9 G. Shen, L. Pan, Z. Lü, C. Wang, F.-e. Aleem, X. Zhang and J.-J. Zou, *Chin. J. Catal.*, 2018, **39**, 920–928.
10 X. Zeng, Z. Wang, G. Wang, T. R. Gengenbach, D. T. McCarthy, A. Deletic, J. Yu and X. Zhang, *Appl. Catal., B*, 2017, **218**, 163–173.
11 L. Ma, G. Wang, C. Jiang, H. Bao and Q. Xu, *Appl. Surf. Sci.*, 2018, **430**, 263–272.
12 S. C. Yan, Z. S. Li and Z. G. Zou, *Langmuir*, 2009, **25**, 10397–10401.
13 Y. Li, H. Zhang, P. Liu, D. Wang, Y. Li and H. Zhao, *Small*, 2013, **9**, 3336–3344.
14 S. Sun, G. Shen, J. Jiang, W. Mi, X. Liu, L. Pan, X. Zhang and J. J. Zou, *Adv. Energy Mater.*, 2019, **9**, 1901505.
15 O. Elbanna, M. Fujitsuka and T. Majima, *ACS Appl. Mater. Interfaces*, 2017, **9**, 34844–34854.
16 L. Song, X. Kang and S. Zhang, *Int. J. Energy Res.*, 2018, **42**, 1649–1656.
17 G. Xu, H. Zhang, J. Wei, H. X. Zhang, X. Wu, Y. Li, C. Li, J. Zhang and J. Ye, *ACS Nano*, 2018, 5333–5340, DOI: 10.1021/acsnano.8b00110.
18 M. Ai, J.-W. Zhang, R. Gao, L. Pan, X. Zhang and J.-J. Zou, *Appl. Catal., B*, 2019, **256**, 117805.
19 S. Sun, Y. Feng, L. Pan, X. Zhang and J.-J. Zou, *Appl. Catal., B*, 2019, **259**, 118028.
20 P. Praus, J. Lang, A. Martaus, L. Svoboda, V. Matějka, M. Kormunda, M. Šihor, M. Reli and K. Kočí, *J. Inorg. Organomet. Polym. Mater.*, 2019, 1219–1234, DOI: 10.1007/s10904-019-01085-4.
21 Y. Han, X. Cao, X. Ouyang, S. P. Sohi and J. Chen, *Chemosphere*, 2016, **145**, 336–341.
22 X. Li, X. Qian, X. An and J. Huang, *Appl. Surf. Sci.*, 2019, **487**, 1262–1270.
23 Y. Li, C. Ji, Y. Lu, L. Wu, S. Sun, R. Qu, C. Sun, Y. Zhang and Z. Xue, *Mater. Chem. Phys.*, 2018, **214**, 28–33.
24 K. Li, Z. Huang, S. Zhu, S. Luo, L. Yan, Y. Dai, Y. Guo and Y. Yang, *Appl. Catal., B*, 2019, **243**, 386–396.
25 X.-K. Ran, X.-T. Wang, P.-P. Liu, Y.-X. Chi, B.-J. Wang, D.-Q. Dou, T.-G. Kang and W. Xiong, *Chin. J. Nat. Med.*, 2013, **11**, 269–273.
26 X. Peng, H. Liu, P. Chen, F. Tang, Y. Hu, F. Wang, Z. Pi, M. Zhao, N. Chen, H. Chen, X. Zhang, X. Yan, M. Liu, X. Fu, G. Zhao, P. Yao, L. Wang, H. Dai, X. Li, W. Xiong, W. Xu, H. Zheng, H. Yu and S. Shen, *Mol. Plant*, 2019, 661–677, DOI: 10.1016/j.molp.2019.01.021.
27 J. S. Cha, S. H. Park, S.-C. Jung, C. Ryu, J.-K. Jeon, M.-C. Shin and Y.-K. Park, *J. Ind. Eng. Chem.*, 2016, **40**, 1–15.
28 K. Weber and P. Quicker, *Fuel*, 2018, **217**, 240–261.
29 V. S. Kosera, T. M. Cruz, E. S. Chaves and E. R. L. Tiburtius, *J. Photochem. Photobiol., A*, 2017, **344**, 184–191.
30 Y.-g. Liu, X.-j. Hu, H. Wang, A.-w. Chen, S.-m. Liu, Y.-m. Guo, Y. He, X. Hu, J. Li, S.-h. Liu, Y.-q. Wang and L. Zhou, *Chem. Eng. J.*, 2013, **226**, 131–138.
31 Y. Ma, J. Wang, S. Xu, S. Feng and J. Wang, *Appl. Surf. Sci.*, 2018, **430**, 155–164.
32 X. Hu, W. Wang, G. Xie, H. Wang, X. Tan, Q. Jin, D. Zhou and Y. Zhao, *Chemosphere*, 2019, **216**, 733–741.
33 G. Qiu, Y. Zhao, H. Wang, X. Tan, F. Chen and X. Hu, *Environ. Sci. Pollut. Res.*, 2019, **26**, 6565–6575.
34 D. Xiao, K. Dai, Y. Qu, Y. Yin and H. Chen, *Appl. Surf. Sci.*, 2015, **358**, 181–187.
35 S. Naeimi and H. Faghihian, *J. Polym. Environ.*, 2019, **27**, 1572–1583.
36 H. W. Kang, S. N. Lim, D. Song and S. B. Park, *Int. J. Hydrogen Energy*, 2012, **37**, 11602–11610.
37 Y. Zhang, Q. Zhang, Q. Shi, Z. Cai and Z. Yang, *Sep. Purif. Technol.*, 2015, **142**, 251–257.
38 Y. Su, Y. Zhao, Y. Zhao, J. Lang, X. Xin and X. Wang, *Appl. Surf. Sci.*, 2015, **358**, 213–222.
39 Y. Shu, C. Tang, X. Hu, L. Jiang, X. Hu and Y. Zhao, *Water*, 2018, **10**, 754–771.
40 H. Wang, X. Yuan, H. Wang, X. Chen, Z. Wu, L. Jiang, W. Xiong and G. Zeng, *Appl. Catal., B*, 2016, **193**, 36–46.
41 W. Dong, S. Chen, S. Jin, M. Chen, B. Yan and Y. Chen, *Propellants, Explos., Pyrotech.*, 2019, **44**, 413–422.
42 Y. Sun, D. Shao, C. Chen, S. Yang and X. Wang, *Environ. Sci. Technol.*, 2013, **47**, 9904–9910.
43 V. H. Tran Thi and B. K. Lee, *J. Hazard. Mater.*, 2017, **324**, 329–339.
44 Y. Deng, L. Tang, G. Zeng, C. Feng, H. Dong, J. Wang, H. Feng, Y. Liu, Y. Zhou and Y. Pang, *Environ. Sci.: Nano*, 2017, **4**, 1494–1511.
45 Y. Liu, X. Yuan, H. Wang, X. Chen, S. Gu, Q. Jiang, Z. Wu, L. Jiang, Y. Wu and G. Zeng, *Catal. Commun.*, 2015, **70**, 17–20.
46 B. A. Manning, J. R. Kiser, H. Kwon and S. R. Kanel, *Environ. Sci. Technol.*, 2007, **41**, 586–592.
47 H. Nguyen Tran, *Chem. Eng. J.*, 2019, **359**, 810–812.